

A cellular solution to a robotics problem

Zitong Jerry Wang^{1*}, Matt Thomson²

¹Center for Interdisciplinary Studies (CIS), School of Science, Westlake University, Zhejiang & 310024, China.

²Division of Biology and Biological Engineering, Caltech, Pasadena & 91125, USA.

*Corresponding author. Email: jerry@westlake.edu.cn

Localizing and navigating toward a signal source in noisy environments remains a fundamental challenge in robotics. Similarly, cells in tissues must navigate noisy, fragmented molecular gradients, shaped by fluid flow and extracellular matrix interactions. We show that cells can perform source localization using a biophysical implementation of a computational algorithm called Bayes filtering, where the spatial distribution of molecules encodes a probability distribution over source location and intracellular transport processes update this distribution. Unlike conventional Bayes filtering, the cellular implementation can adjust the weight of past observations based on current environmental signals. When translated to traditional robotics algorithms, this signal-aware learning rate significantly improves navigation performance in high-noise conditions, revealing how biological mechanisms can advance engineered systems.

Localizing and navigating toward a target in a complex, noisy environment is a fundamental challenge in robotics. Over the past several decades, Bayes filtering and its variants—Kalman filters, particle filters, and smoothing-based methods—have become standard tools for robotic state estimation and navigation tasks ranging from self-driving cars to drone flight control (1). These Bayesian approaches iteratively update a belief distribution over the target location using sensor measurements. Bayes filtering leads to optimal estimates of the true target location in the sense of

having the smallest mean squared error under standard assumptions. Despite their success, high-noise conditions and significant variability in motion can still degrade performance, especially in unstructured or rapidly changing environments (2).

Cells can efficiently localize to ligand sources in complex tissue environments, but the mechanisms remain unclear. In tissues, extracellular matrix (ECM) binding and interstitial fluid flow break ligand gradients into irregular, fragmented patches (3–6). For example, CCL21 secreted from lymphatic vessels in the dermal interstitium is transported by fluid flow and captured by a non-uniform ECM network, forming a stable, reticulated pattern with local concentration peaks (6). Similar phenomena have been observed for other guidance molecules *in vivo* (7–9). As a result, cells below 40 μm in diameter often experience local gradients that do not reliably point toward the true source (6). A naive gradient-following strategy would risk trapping cells at these signal peaks, preventing efficient source localization. Meanwhile, random walks are similarly inefficient over long distances due to the slow speed of cell migration. Understanding how cells navigate such noisy, complex environments may suggest new strategies to improve robotic algorithms.

Recent observations suggest dynamic spatial rearrangement of surface receptors may be important for effective navigation. For instance, receptors such as TrkB, Robo1, and PlxnA1 in neuronal growth cones reorganize according to local ligand distributions, and inhibiting their rearrangement impairs directional guidance (10, 11). Similarly, blocking CCR2 receptor redistribution on mesenchymal stem cells, without changing its overall expression, severely disrupts targeted migration to injured muscle tissues (12). These observations suggest that receptor dynamics—not just expression—can be pivotal for robust navigation.

In this work, we show that dynamic receptor rearrangement can function as a biophysical implementation of a Bayes filter that is optimized for tissue navigation. The spatial distribution of receptors encodes a probability distribution over source location and intracellular transport processes update this distribution based on local ligand cues. Unlike conventional Bayes filtering, the cellular Bayes filter can adjust the weight of past observations in response to current signals. We demonstrate, through simulations, that translating this adaptive mechanism back into traditional robotics algorithms yields significantly improved source localization in high-noise and high-variance motion scenarios. Our results illustrate how biological mechanisms can inspire more robust navigation solutions in engineered systems.

Naive gradient tracking is insufficient for interstitial gradients

Cells navigate to a ligand source by tracking local concentration gradients, but the local gradient does not always point toward the ligand source. For example, CCL21 is a chemokine secreted by lymphatic endothelial cells that guides dendritic cells toward lymphatic vessels. Quantitative imaging of mouse ear dermis reveals gradients of CCL21 within the perilymphatic interstitium when averaged across multiple spatial regions (Figure 1A, adopted from (6)). However, these chemokines are distributed in disconnected patches, leading typical immune cells ($10\text{-}20 \mu\text{m}$ in diameter) to observe local gradient directions that often fail to align with the global source direction (Figure 1B).

We show through PDE simulation of fluid flow through an ECM matrix that such a patchy distribution can be partly explained by the irregular network of ECM proteins (13). Indeed, our simulated ligand distribution closely resembles experimentally observed chemokine distributions (Figure 1A-B). In both cases, local gradient directions experienced by a typical immune cell ($10\text{-}20 \mu\text{m}$ in diameter) fail to align with the global gradient direction, whereas larger cells ($40\mu\text{m}$) do not experience this misalignment (Figure 1B).

We simulated cells migrating in patchy interstitial gradients and found that cells consistently become trapped in local ligand patches when strictly following local gradients (Figure 1C-D). We implement local gradient tracking by repeatedly computing receptor activity across a cell's membrane and translating the cell in the direction of maximal receptor activity (13). Figure 1C demonstrates how simulated cell trajectories tend to become trapped away from the ligand source. As predicted by the gradient vector fields in Figure 1B, cells ($10\text{-}20 \mu\text{m}$ in diameter) fail to traverse a $50 \mu\text{m}$ gradient even after six hours (Figure 1D). This problem is analogous to the challenge of designing optimization algorithms for non-convex functions with local optima, where naive gradient descent strategies provably fail to reach the global optimum.

Cell navigation as a Bayesian inference problem

We formulate cell target tracking as a spatial Bayesian inference problem, drawing inspiration from Bayes filtering in robotic source localization. Instead of moving in the direction of the highest ligand concentration, a Bayesian strategy requires the cell to maintain a "belief" over the target

direction as a probability distribution and move in the direction of the strongest belief (Figure 2A).

Bayes filtering is a probabilistic technique for estimating the state of a system over time by iteratively updating predictions with new observations (1). In robotic localization (Figure 2A), Bayes filtering helps the agent estimate a target's location at time t , denoted θ_t , by maintaining a probability distribution, $\text{bel}(\theta_t)$, over all possible locations. This estimate is iteratively refined using new input signals Z_t according to the following update rule:

$$\text{bel}(\theta_t) = \eta p(Z_t | \theta_t) \int_{-\pi}^{\pi} p(\theta_t | \theta_{t-1}) \text{bel}(\theta_{t-1}) d\theta_{t-1}. \quad (1)$$

Here, $p(Z_t | \theta_t)$ is the observation model, which updates the agent's belief about the target's location by incorporating newly acquired signals Z_t . The term $p(\theta_t | \theta_{t-1})$ is the motion model, which predicts how the agent's or target's position evolves over time based on known actions or movement patterns (Figure 2B). It accounts for uncertainties in movement and projects the distribution forward, updating the agent's belief even before any new signals have been observed. At each time step after updating its belief distribution, the agent moves in the direction with the highest probability, maximizing its likelihood of locating the target.

We can map Bayes filtering to our cell navigation problem by specifying both the observation model and the motion model. In cell navigation, we define θ_t as one of N possible directions of the ligand source relative to the cell, given by $\theta_t = \frac{2\pi i}{N}$ for $i = 1, \dots, N$. The belief distribution $\text{bel}\left(\theta_t = \frac{2\pi i}{N}\right)$ is denoted as P_i^t , and the input signal is the vector of ligand counts $C_t \in \mathbb{Z}^N$ around the cell. The observation model $p(C_t | \theta_t)$ represents the likelihood of the cell observing ligand distribution C_t given a source direction θ_t . For simplicity, we assume a local observation models where $p(C_t | \theta_t)$ depends only on $C_t(\theta_t)$, the ligand level at direction θ_t . Sampling from our simulated interstitial gradient, we show that we can approximate the observation model as:

$$p(C_t | \theta_t = 2\pi i / N) \approx \eta(1 + \beta C_i^t) \quad (2)$$

where $C_i^t = C_t(\theta_t = 2\pi i / N)$. For the motion model, we use an odometry-based Gaussian noise model, assuming

$$\theta_t | \theta_{t-1} \sim \mathcal{N}(\theta_{t-1}, \sigma^2)$$

with $\sigma^2 \ll 1$, a common approach in robotic navigation. This noise represents fluctuations in the direction of a cell's movement. Under these assumptions, the integral in Equation 1 reduces to

a simple sum:

$$\int_{-\pi}^{\pi} p(\theta_t | \theta_{t-1}) \text{bel}(\theta_{t-1}) d\theta_{t-1} \approx \sigma(P_{i-1}^{t-1} + P_{i+1}^{t-1}) + (1 - 2\sigma)P_i^{t-1} \quad (3)$$

Altogether, we obtain the cellular Bayes filter update equation,

$$P_i^t = \eta (1 + \beta C_i^t) \left[\sigma(P_{i-1}^{t-1} + P_{i+1}^{t-1}) + (1 - 2\sigma)P_i^{t-1} \right] \quad (4)$$

This process allows cells to iteratively refine predictions with observations, enabling robust tracking and localization in unpredictable environments. Indeed, Figure 2C shows that cells simulated to move in the direction of maximal probability, using Bayes updates according to Equation 4, navigate interstitial gradients with a 30-fold higher success rate compared to simple gradient tracking.

Adaptive receptor redistribution acts as a Bayes filter for efficient navigation

For a cell to implement Bayes filtering, it minimally requires a physical substrate to store the belief distribution $P(\theta_t)$ (Figure 3A). The motion model in Equation 3 requires this substrate to diffuse in 2D for a 3D cell, while the observation model in Equation 2 requires it to interact directly with signaling ligands. Cell surface receptors fulfill both requirements. Figure 3B shows that activity-dependent receptor rearrangement implements an exact Bayes filter by mapping the observation model parameter (β) to biased receptor exocytosis, the motion model parameter (σ) to membrane diffusion, and the normalization constant (η) to receptor endocytosis (13).

Altogether, these mappings show that the cellular Bayes filter update rule (Equation 4) is mathematically equivalent to receptor dynamics described by the following PDE,

$$\frac{\partial R(x, t)}{\partial t} = D \nabla_{\text{memb}}^2 R - k_{\text{off}} R + h A R_{\text{cyto}} \quad (5)$$

Figure 3C illustrates each component of these receptor dynamics, where k_{off} is the rate of receptor endocytosis, hA represents the rate of receptor exocytosis which scales with local receptor activity A , and D is the membrane diffusion coefficient. Kymograph comparisons in Figure 3D confirm that, when using match parameter values, the spatiotemporal dynamics of receptors $R(x, t)$ exactly match those of the probability distribution $P(\theta_t)$ evolving through recursive Bayesian updates. Note that activity-dependent rearrangement of cell surface receptors has been observed across

multiple migratory cell types, including lymphocytes (14, 15), carcinoma cells (16), mesenchymal stem cells (12), and growth cones (10, 17, 18), where polarized exocytosis has been observed for some of these receptors (17–20).

Simulated cells with active receptor redistribution rapidly localize to the ligand source, effectively avoiding ligand patches in interstitial gradients. To assess navigation efficiency, we simulated cells navigating an interstitial gradient with the goal of attempting to reach the ligand source located at the left boundary (Figure 3E). We compared navigation efficiency of three cellular strategies: uniform, feedback and LEGI (Methods). The uniform strategy corresponds to naive gradient ascent, where cells simply follow the direction of maximal receptor activity. In the feedback strategy, cells also follow the direction of maximal receptor activity, but receptors actively redistribute according to the dynamics described by Equation 5. The Local Excitation and Global Inhibition (LEGI) strategy (21) is a mechanism where cells respond to nearby signals by amplifying local signaling (excitation) at the cell's front while simultaneously inhibiting signal sensitivity across the rest of the cell, allowing directed movement toward the signal source. For 10-20 μm cells, Figure 3E shows cells with active receptor redistribution successfully localize to the ligand source efficiently, overcoming local ligand patches. In contrast, both the uniform and LEGI strategies fail to cross the 60 μm gradient even after three hours (Figure 3F). Simulation of both the feedback and LEGI strategy used physiologically plausible parameters from literature (20, 21).

Bayesian formalism predicts cell constraints

The equivalence between the Bayesian formulation and the PDE formulation predicts coupling between cell speed, cell signaling, and spatial structure of the tissue signaling environment.

In standard robotic Bayes filter, the motion model noise σ increases with agent speed (Equation 3). This connection accounts for the fact that as an agent moves faster, the uncertainty in its future position increases because small errors in estimating direction have a larger effect over the traveled distance. Mapping motion model to receptor dynamics (Figure 3B) links σ to receptor diffusivity, predicting that optimal receptor diffusion depends on cell speed. Figure 4A-B confirms this relationship, showing that higher cell speeds require greater receptor diffusivity. Intuitively, a fast-moving cell must reset its priors more frequently as its environment changes faster. Lastly,

Figure 4A suggests that low receptor diffusivity alone appears sufficient for efficient migration rather than strict adherence to Figure 4B's monotonic trend.

In the observation model of a Bayes filter (Equation 2), β reflects the patchiness of the interstitial gradient. Its mapping to the receptor PDE (Figure 3B) suggests that optimal receptor transport depends on environmental patchiness. Figure 4C shows that reducing ECM binding shifts the gradient from ECM-bound to soluble, decreasing patchiness. In soluble gradients, where local and global gradient directions align, higher receptor transport enables faster target localization (Figure 4D). Notably, in these conditions, Bayes filtering may be unnecessary, as simple gradient tracking suffices. Indeed, C5aR, a receptor that does not adaptively redistribute, binds soluble ligands that lack ECM binding (22, 23).

Biological implementation improves standard algorithm

A unique feature of cellular Bayesian filtering, distinct from standard implementations in robotics, is the coupling between observed signals and the motion model. In traditional Bayesian filtering, the motion model accounts for uncertainty in movement (e.g., slippage, wind) and is independent of the observed signal dynamics. However, many membrane receptors, including chemokine receptors, deviate from this paradigm: their diffusivity (motion model variance) is modulated by ligand binding (observed signal). Figure 5A illustrates multiple biophysical mechanisms that reduce receptor diffusivity upon ligand binding, including oligomerization (24), lipid raft association (10), and cytoskeletal anchoring (25).

This activity-dependent coupling enhances Bayesian filtering for target localization in noisy environments. To assess potential effects of this coupling (Figure 5B), we compare two agents navigating toward a signal source (star): one using fixed variance in its motion model and another using adaptive variance. In the absence of any signal, both use a baseline variance D_{true} , the actual motion noise. However, in the presence of a signal, the adaptive agent exponentially reduces variance with increasing signal strength s ,

$$D := D_0 + (D_{\text{true}} - D_0) \exp(-ks),$$

where $D_0 < D_{\text{true}}$. Figure 5C shows that adaptive variance reduces the time-to-target by a factor

of four or more, with the greatest benefit observed in low signal-to-noise ratio (SNR) environments. This improvement follows from Kalman filter gain analysis (13). When the agent is far from the target and the signal is weak, a higher D keeps the belief more responsive to new, noisy measurements, preventing the filter from becoming overly reliant on an uncertain prior. Conversely, near the target, where the signal is strong, reducing D locks in past reliable estimates, accelerating convergence. The adaptive strategy is particularly advantageous in low-SNR environments, where weak signals and high measurement uncertainty otherwise hinder belief updates.

Discussion

In this work, we investigated cell navigation in patchy interstitial gradients and established a direct mapping between activity-dependent receptor redistribution and Bayesian filtering, a widely used robotic navigation algorithm. This mapping demonstrates that adaptive receptor redistribution can enable cells to efficiently navigate interstitial gradients, overcoming localized signal patchiness. Furthermore, it reveals a unique feature of the cellular Bayesian filter, the coupling between signal detection and receptor dynamics, that enhances standard Bayesian filtering in robotic navigation.

Alternative implementations of a Bayes filter that does not require receptor redistribution are possible. For example, we may reinterpret $R(x, t)$ as the number of sensitive receptors at membrane position x and time t instead of absolute receptor count. In such a case, receptor sensitivity may be determined by some biochemical modification of receptors which can spread to nearby receptors. Another alternative is storing the belief distribution downstream of receptor activation, where the observed signal corresponds to receptor activation rather than ligand concentration. The same Bayesian framework applies to any membrane-bound molecule involved in signal processing.

The connection between Bayes filtering and receptor redistribution suggests an interesting hypothesis for receptors that bind either ECM-bound ligands compared to soluble ligands. Specifically, our model suggests that receptors that binds ECM-bound signal would benefit more strongly from adaptive redistribution compared to receptors that mostly interacts with soluble signals. Further experimental validation is needed to test this prediction and explore its biological implications.

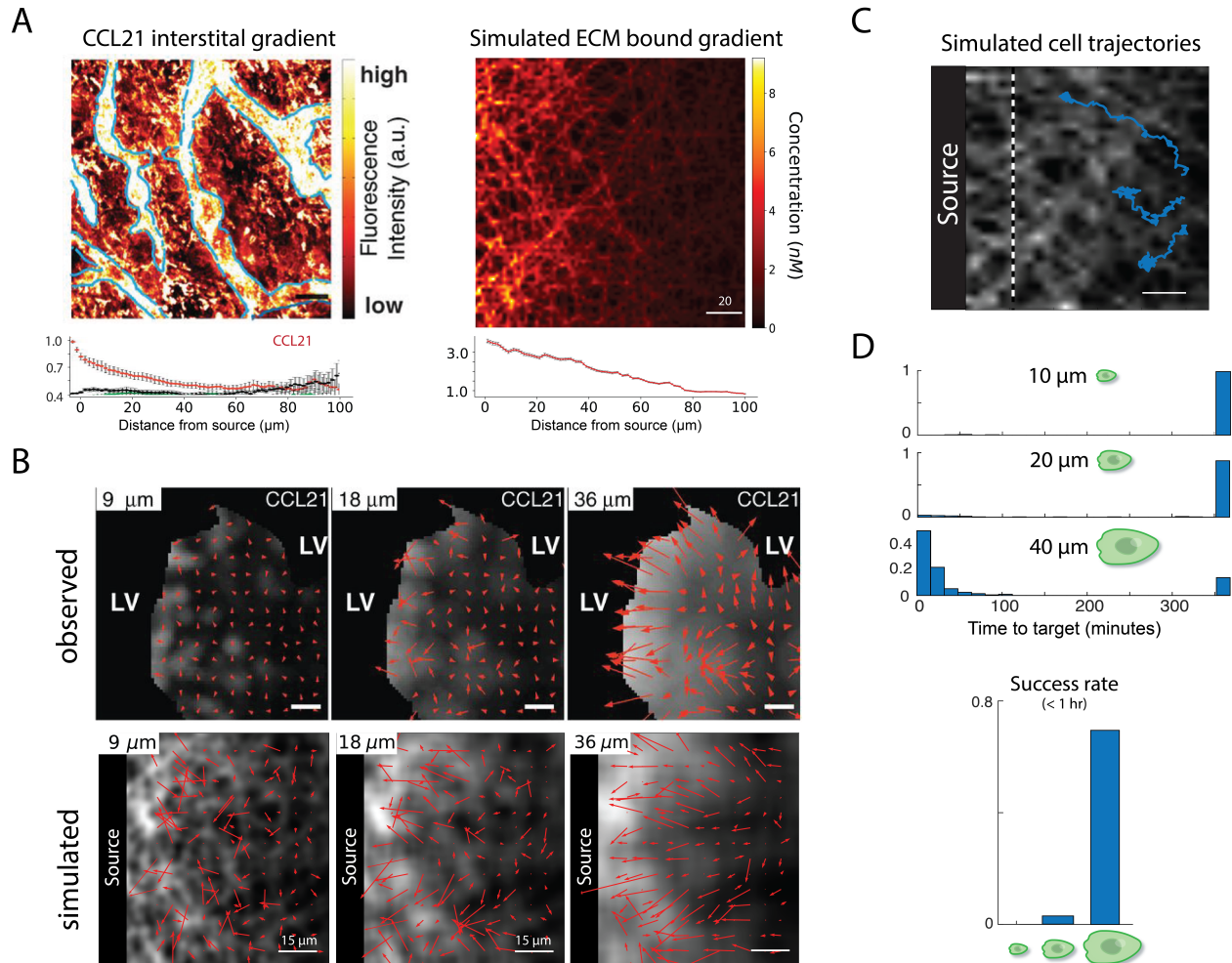
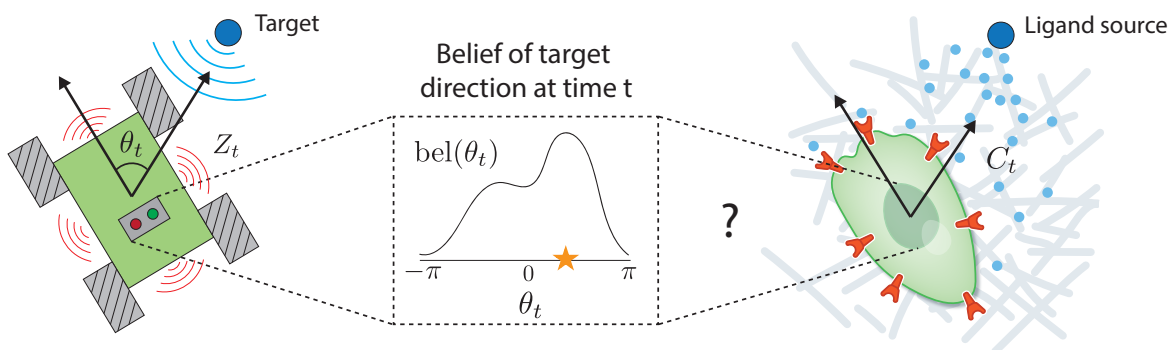


Figure 1: Cell migration in interstitial chemokine gradient. (A) Observed CCL21 gradient in the mouse ear dermis (left) and simulated ECM-bound gradient (right), with their respective average concentrations shown below. (B) Observed and simulated interstitial chemokine distributions, with vector fields showing the local gradient directions as experienced by cells of sizes 9, 18, and 36 μm . (C) Simulated cell trajectories for cells migrating strictly along the local gradient at a speed of 2 $\mu\text{m}/\text{min}$ for 6 hours. (D) Time to reach the ligand source for simulated cells of different sizes. Success rate is defined as the proportion of cells reaching the ligand source within 1 hour. CCL21 images adapted from (6).

A



B

General Bayesian filter update equation

$$\text{bel}(\theta_t) = \frac{\eta p(Z_t | \theta_t)}{\text{Observation model}} \int_{-\pi}^{\pi} \frac{p(\theta_t | \theta_{t-1}) \text{bel}(\theta_{t-1})}{\text{Motion model}} d\theta_{t-1}$$

\Downarrow

$$\text{bel}(\theta_t = \frac{\pi i}{N}) = P_i^t$$

Cellular Bayesian filter update equation

$$P_i^t = \eta(1 + \beta C_i^t) \left[\sigma(P_{i-1}^{t-1} + P_{i+1}^{t-1}) + (1 - 2\sigma)P_i^{t-1} \right]$$

$\frac{\text{Learned from tissue images}}{\text{Based on cell motion}}$

C

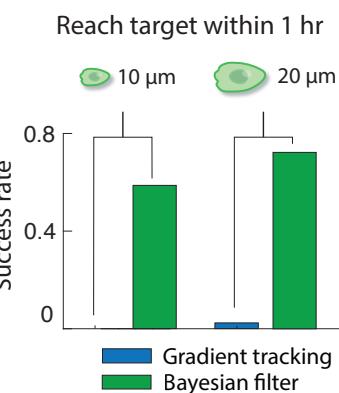


Figure 2: Mapping cell navigation to Bayes filtering. (A) Bayes filtering maintains a belief distribution over possible target directions, and agent moves in the direction of maximum belief (star). (B) The general Bayes filter update equation consists of both an observation model and a motion model, which we map onto the cell navigation problem. (C) Success rate of cells simulated to navigate with simple gradient tracking where the cell consistently moves in the direction of local gradient compared to cells updating a belief distribution via the cellular Bayes filter from panel (B) and moving in the direction of maximal belief.

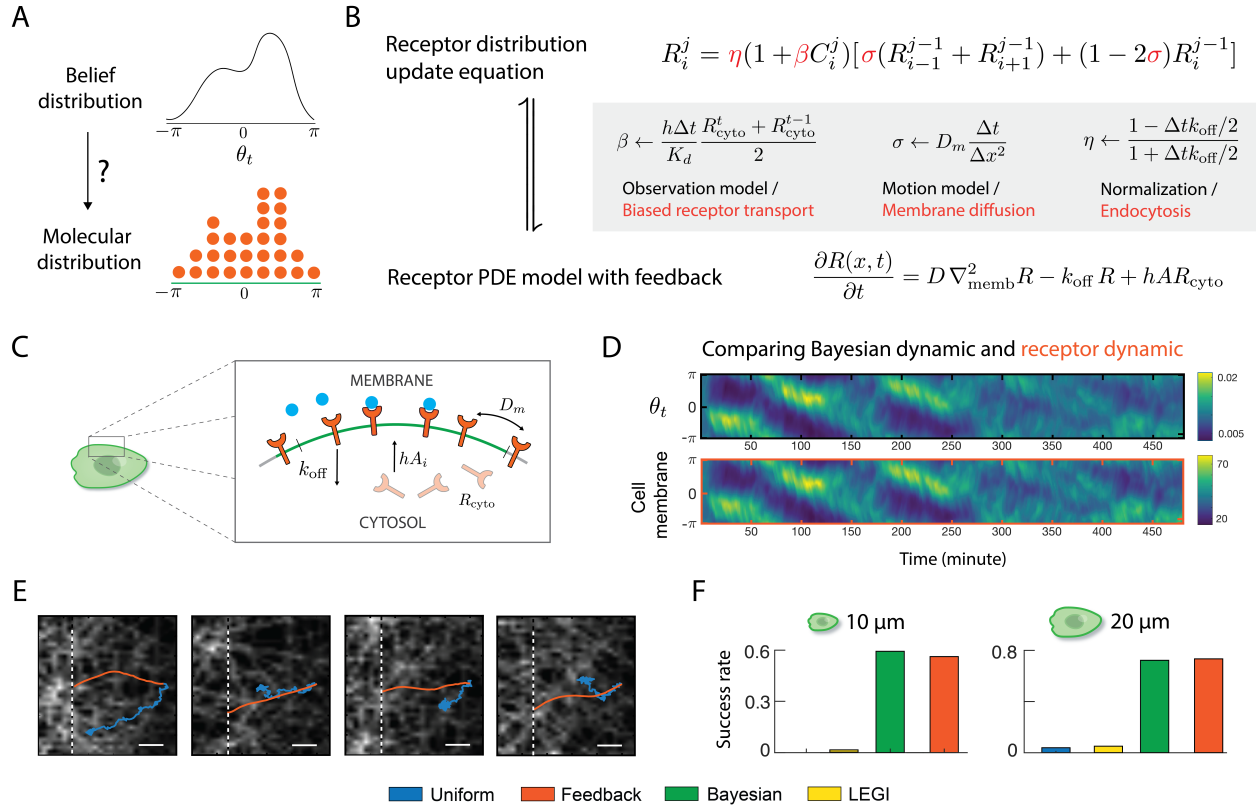


Figure 3: Mapping Bayes filtering to receptor dynamics. (A) Conceptual mapping of a mathematical belief distribution to a physical distribution of molecules. (B) Mathematical equivalence between the Bayesian update equation and a receptor PDE model. (C) Schematic of the receptor PDE model, illustrating key molecular processes. (D) Kymograph comparison of the evolving Bayesian belief distribution and the simulated receptor distribution in response to the same dynamically changing environment. (E) Simulated cell trajectories with and without active receptor redistribution. (F) Navigation performance, showing time to source and success rate for cells using uniform receptors, actively redistributed receptors, Bayesian filter updates, and Local Excitation Global Inhibition (LEGI) strategies.

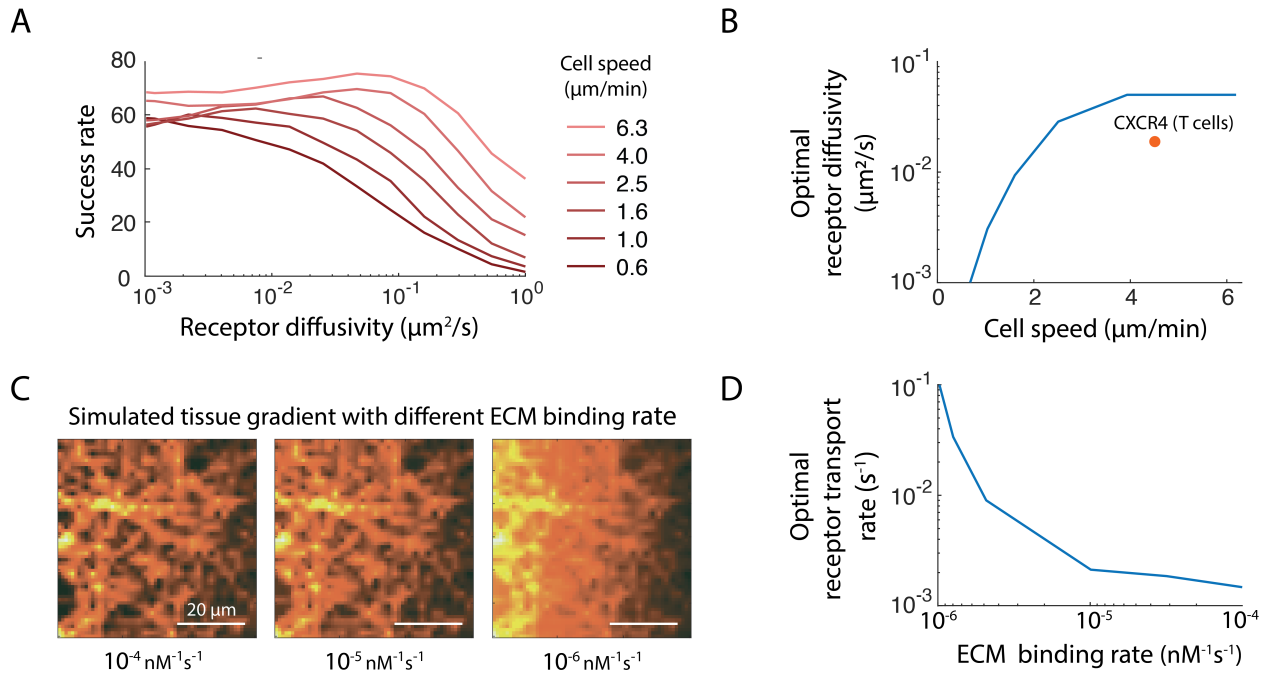


Figure 4: Bayesian formalism predicts optimal receptor dynamics. (A) Success rate for cells simulated with different receptor diffusivity and cell speed. (B) Optimal receptor diffusivity at various cell speed, dot showing empirical data for CXCR4 (26) and T cells (27). (C) Simulated interstitial gradient formed by ligands with different ECM binding rate, given continuous ligand secretion. (D) Optimal receptor transport rate (coefficient) at various ligand-ECM binding rates.

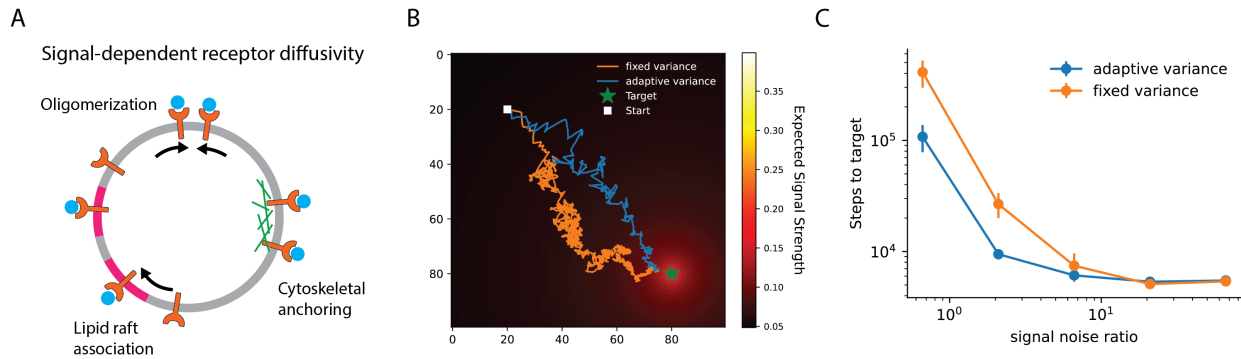


Figure 5: Signal-coupled motion model for robotic target navigation. (A) Example cellular mechanisms which couples receptor activation with receptor diffusivity (motion model variance). (B) Simulated trajectories of robotic agent attempting a target navigation task, either with or without signal coupling to motion model. (C) Navigation efficiency of the two different strategies in environments with different signal-to-noise ratio (SNR).

References and Notes

1. V. Fox, J. Hightower, L. Liao, D. Schulz, G. Borriello, Bayesian filtering for location estimation. *IEEE Pervasive Computing* **2** (3), 24–33 (2003), doi:10.1109/MPRV.2003.1228524.
2. Y. Cheng, S. Zhang, X. Wang, H. Wang, Self-Tuning Process Noise in Variational Bayesian Adaptive Kalman Filter for Target Tracking. *Electronics* **12** (18), 3887 (2023).
3. D. J. Fowell, M. Kim, The spatio-temporal control of effector T cell migration. *Nature Reviews Immunology* pp. 1–15 (2021).
4. E. Russo, *et al.*, Intralymphatic CCL21 promotes tissue egress of dendritic cells through afferent lymphatic vessels. *Cell reports* **14** (7), 1723–1734 (2016).
5. A. C. von Philipsborn, *et al.*, Growth cone navigation in substrate-bound ephrin gradients. *Development* **133** (13), 2487–2495 (2006).
6. M. Weber, *et al.*, Interstitial dendritic cell guidance by haptotactic chemokine gradients. *Science* **339** (6117), 328–332 (2013).
7. T. E. Kennedy, H. Wang, W. Marshall, M. Tessier-Lavigne, Axon guidance by diffusible chemoattractants: a gradient of netrin protein in the developing spinal cord. *Journal of Neuroscience* **26** (34), 8866–8874 (2006).
8. M. Sarris, *et al.*, Inflammatory chemokines direct and restrict leukocyte migration within live tissues as glycan-bound gradients. *Current Biology* **22** (24), 2375–2382 (2012).
9. E. Donà, *et al.*, Directional tissue migration through a self-generated chemokine gradient. *Nature* **503** (7475), 285–289 (2013).
10. C. Guirland, S. Suzuki, M. Kojima, B. Lu, J. Q. Zheng, Lipid rafts mediate chemotropic guidance of nerve growth cones. *Neuron* **42** (1), 51–62 (2004).
11. A. Pignata, *et al.*, A spatiotemporal sequence of sensitization to slits and semaphorins orchestrates commissural axon navigation. *Cell reports* **29** (2), 347–362 (2019).

12. F. Belema-Bedada, S. Uchida, A. Martire, S. Kostin, T. Braun, Efficient homing of multipotent adult mesenchymal stem cells depends on FROUNT-mediated clustering of CCR2. *Cell stem cell* **2** (6), 566–575 (2008).
13. Materials and methods are available as supplementary material.
14. M. Vicente-Manzanares, *et al.*, The chemokine SDF-1 α triggers a chemotactic response and induces cell polarization in human B lymphocytes. *European journal of immunology* **28** (7), 2197–2207 (1998).
15. M. Shimonaka, *et al.*, Rap1 translates chemokine signals to integrin activation, cell polarization, and motility across vascular endothelium under flow. *The Journal of cell biology* **161** (2), 417–427 (2003).
16. S. Mañes, *et al.*, Membrane raft microdomains in chemokine receptor function, in *seminars in IMMUNOLOGY* (Elsevier), vol. 13 (2001), pp. 147–157.
17. C. Bouzigues, M. Morel, A. Triller, M. Dahan, Asymmetric redistribution of GABA receptors during GABA gradient sensing by nerve growth cones analyzed by single quantum dot imaging. *Proceedings of the National Academy of Sciences* **104** (27), 11251–11256 (2007).
18. T. Tojima, *et al.*, Attractive axon guidance involves asymmetric membrane transport and exocytosis in the growth cone. *Nature neuroscience* **10** (1), 58–66 (2007).
19. V. Das, *et al.*, Activation-induced polarized recycling targets T cell antigen receptors to the immunological synapse: involvement of SNARE complexes. *Immunity* **20** (5), 577–588 (2004).
20. A. W. McClure, *et al.*, Role of polarized G protein signaling in tracking pheromone gradients. *Developmental cell* **35** (4), 471–482 (2015).
21. Y. Xiong, C.-H. Huang, P. A. Iglesias, P. N. Devreotes, Cells navigate with a local-excitation, global-inhibition-biased excitable network. *Proceedings of the National Academy of Sciences* **107** (40), 17079–17086 (2010).

22. G. Servant, O. D. Weiner, E. R. Neptune, J. W. Sedat, H. R. Bourne, Dynamics of a chemoattractant receptor in living neutrophils during chemotaxis. *Molecular biology of the cell* **10** (4), 1163–1178 (1999).
23. Z. Xiao, N. Zhang, D. B. Murphy, P. N. Devreotes, Dynamic distribution of chemoattractant receptors in living cells during chemotaxis and persistent stimulation. *The Journal of cell biology* **139** (2), 365–374 (1997).
24. S. Gahbauer, R. A. Böckmann, Membrane-mediated oligomerization of G protein coupled receptors and its implications for GPCR function. *Frontiers in physiology* **7**, 494 (2016).
25. L. Martínez-Muñoz, *et al.*, Separating actin-dependent chemokine receptor nanoclustering from dimerization indicates a role for clustering in CXCR4 signaling and function. *Molecular cell* **70** (1), 106–119 (2018).
26. D. J. Torres, *et al.*, Quantitative analyses of T cell motion in tissue reveals factors driving T cell search in tissues. *Elife* **12**, e84916 (2023).
27. E. M. García-Cuesta, *et al.*, Allosteric modulation of the CXCR4: CXCL12 axis by targeting receptor nanoclustering via the TMV-TMVI domain. *Elife* **13**, RP93968 (2024).
28. K. A. Rejniak, *et al.*, The role of tumor tissue architecture in treatment penetration and efficacy: an integrative study. *Frontiers in oncology* **3**, 111 (2013).
29. F. Milde, M. Bergdorf, P. Koumoutsakos, A hybrid model for three-dimensional simulations of sprouting angiogenesis. *Biophysical journal* **95** (7), 3146–3160 (2008).
30. X. Wang, M. R. Lennartz, D. J. Loegering, J. A. Stenken, Multiplexed cytokine detection of interstitial fluid collected from polymeric hollow tube implants—a feasibility study. *Cytokine* **43** (1), 15–19 (2008).
31. K. E. Clark, *et al.*, Multiplex cytokine analysis of dermal interstitial blister fluid defines local disease mechanisms in systemic sclerosis. *Arthritis research & therapy* **17** (1), 1–11 (2015).
32. D. Harjanto, M. H. Zaman, Modeling extracellular matrix reorganization in 3D environments. *PLoS One* **8** (1), e52509 (2013).

33. D. K. Schlüter, I. Ramis-Conde, M. A. Chaplain, Computational modeling of single-cell migration: the leading role of extracellular matrix fibers. *Biophysical journal* **103** (6), 1141–1151 (2012).
34. B. Lee, *et al.*, A three-dimensional computational model of collagen network mechanics. *PloS one* **9** (11), e111896 (2014).
35. P. Friedl, *et al.*, Migration of highly aggressive MV3 melanoma cells in 3-dimensional collagen lattices results in local matrix reorganization and shedding of $\alpha 2$ and $\beta 1$ integrins and CD44. *Cancer research* **57** (10), 2061–2070 (1997).
36. M. Ueda, Y. Sako, T. Tanaka, P. Devreotes, T. Yanagida, Single-molecule analysis of chemo-tactic signaling in Dictyostelium cells. *Science* **294** (5543), 864–867 (2001).
37. E. Marco, R. Wedlich-Soldner, R. Li, S. J. Altschuler, L. F. Wu, Endocytosis optimizes the dynamic localization of membrane proteins that regulate cortical polarity. *Cell* **129** (2), 411–422 (2007).
38. B. Hegemann, *et al.*, A cellular system for spatial signal decoding in chemical gradients. *Developmental cell* **35** (4), 458–470 (2015).
39. L. D. L. JJ, Receptors: Models for binding, trafficking, and signaling (1993).
40. S. Pippig, S. Andexinger, M. J. Lohse, Sequestration and recycling of beta 2-adrenergic receptors permit receptor resensitization. *Molecular pharmacology* **47** (4), 666–676 (1995).
41. J. A. Koenig, J. M. Edwardson, Intracellular trafficking of the muscarinic acetylcholine receptor: importance of subtype and cell type. *Molecular pharmacology* **49** (2), 351–359 (1996).
42. J. A. Koenig, J. M. Edwardson, Kinetic analysis of the trafficking of muscarinic acetylcholine receptors between the plasma membrane and intracellular compartments. *Journal of Biological Chemistry* **269** (25), 17174–17182 (1994).
43. C. Shi, C.-H. Huang, P. N. Devreotes, P. A. Iglesias, Interaction of motility, directional sensing, and polarity modules recreates the behaviors of chemotaxing cells. *PLoS computational biology* **9** (7), e1003122 (2013).

44. MATLAB, 23.2.0.2409890 (*R2023b*) (The MathWorks Inc., Natick, Massachusetts) (2023).

Acknowledgments

We would like to thank Pablo Iglesias for providing the LEGI-BEN simulation code.

Funding: Z. J. W. was funded by the Westlake Fellows program provided by Westlake University.

Author contributions: Z. J. W. conceived the idea and performed all simulation and mathematical analysis. Z. J. W. and M. T. wrote the paper. Both Z. J. W. and M.T. provided funding for the project.

Competing interests: There are no competing interests to declare.

Data and materials availability: The code used in this study is publicly available on GitHub at [cellethology/bayesian-cell](#). This repository contains all scripts and instructions necessary to reproduce the primary results presented in the paper.

Supplementary materials

Materials and Methods

Supplementary Materials for A cellular solution to a robotics problem

Zitong Jerry Wang*, Matt Thomson

*Corresponding author. Email: jerry@westlake.edu.cn

This PDF file includes:

Materials and Methods

Materials and Methods

Derivation of equivalence between receptor PDE and Bayes filtering

The original discrete update equation is given as:

$$P_i^{t+1} - P_i^t = \eta(1 + \beta C_i^t) \left[\sigma(P_{i-1}^t + P_{i+1}^t) + (1 - 2\sigma)P_i^t \right] - P_i^t.$$

Rewriting and expanding:

$$P_i^{t+1} - P_i^t = \eta\sigma(P_{i-1}^t + P_{i+1}^t) + \eta(1 - 2\sigma)P_i^t + \eta\beta C_i^t \left[\sigma(P_{i-1}^{t-1} + P_{i+1}^t) + (1 - 2\sigma)P_i^t \right] - P_i^t.$$

Grouping terms:

$$P_i^{t+1} - P_i^t = \eta\sigma(P_{i-1}^t + P_{i+1}^t - 2P_i^t) + (\eta - 1)P_i^t + \eta\beta C_i^t \left[\sigma(P_{i-1}^{t-1} + P_{i+1}^t) + (1 - 2\sigma)P_i^t \right].$$

Replacing P_i with R_i and dividing by Δt , we get:

$$\frac{R_i^{t+1} - R_i^t}{\Delta t} = \frac{\eta}{\Delta t}\sigma(R_{i-1}^t + R_{i+1}^t - 2R_i^t) + \frac{\eta - 1}{\Delta t}R_i^t + \frac{\eta}{\Delta t}\beta C_i^t \left[\sigma(R_{i-1}^{t-1} + R_{i+1}^t) + (1 - 2\sigma)R_i^t \right].$$

(a) Diffusion Term Mapping The first term:

$$\frac{\eta}{\Delta t}\sigma(R_{i-1}^t + R_{i+1}^t - 2R_i^t)$$

maps to diffusion. Given $\sigma = D_m \frac{\Delta t}{\Delta x^2}$ and $\eta \approx 1$ for small Δt , we simplify:

$$\frac{\eta}{\Delta t}\sigma(R_{i-1}^t + R_{i+1}^t - 2R_i^t) = \eta D_m \frac{\Delta t}{\Delta x^2} \frac{(R_{i-1}^t + R_{i+1}^t - 2R_i^t)}{\Delta t}.$$

Cancelling Δt :

$$\eta D_m \frac{(R_{i-1}^t + R_{i+1}^t - 2R_i^t)}{\Delta x^2} \rightarrow D_m \nabla_{\text{memb}}^2 R.$$

(b) Decay Term Mapping The second term:

$$\frac{\eta - 1}{\Delta t}R_i^t$$

maps to receptor endocytosis. Given $\eta = \frac{1 - \Delta t k_{\text{off}}/2}{1 + \Delta t k_{\text{off}}/2}$:

$$\frac{\eta - 1}{\Delta t} = \frac{1}{\Delta t} \left(\frac{1 - \Delta t k_{\text{off}}/2}{1 + \Delta t k_{\text{off}}/2} - 1 \right).$$

Simplifying:

$$\frac{\eta - 1}{\Delta t} = \frac{-\Delta t k_{\text{off}}}{\Delta t (1 + \Delta t k_{\text{off}}/2)} \rightarrow -k_{\text{off}} \quad \text{as } \Delta t \rightarrow 0.$$

Thus:

$$\frac{\eta - 1}{\Delta t} R_i^t \rightarrow -k_{\text{off}} R_i^t.$$

(c) Binding Term Mapping The last term:

$$\frac{\eta}{\Delta t} \beta C_i^t \left[\sigma(R_{i-1}^t + R_{i+1}^t) + (1 - 2\sigma) R_i^t \right]$$

maps to receptor membrane transport. Given $\beta = \frac{h\Delta t}{K_d} \frac{R_{\text{cyto}}^{t+1} + R_{\text{cyto}}^t}{2}$ and $A = \frac{R_i^t C_i^t}{K_d}$, we get:

$$\frac{h}{K_d} \frac{R_{\text{cyto}}^{t+1} + R_{\text{cyto}}^t}{2} C_i^t \left[\sigma(R_{i-1}^t + R_{i+1}^t) + (1 - 2\sigma) R_i^t \right],$$

where $\eta \rightarrow 1$ as $\Delta t \rightarrow 0$. Now, consider $\Delta x \rightarrow 0$, we can simplify this expression further

$$h A_i^t \frac{R_{\text{cyto}}^{t+1} + R_{\text{cyto}}^t}{2}.$$

where $A_i^t = \frac{R_i^t C_i^t}{K_d}$. This is the semi-implicit treatment of hAR_{cyto} using the Crank-Nicolson method.

Finally, combining the terms, the final continuous-time PDE is:

$$\frac{\partial R(x, t)}{\partial t} = D_m \nabla_{\text{memb}}^2 R(x, t) - k_{\text{off}} R(x, t) + hAR_{\text{cyto}},$$

where $A = \frac{R(x,t)C(x,t)}{K_d}$.

Institutional gradient simulation

We follow mathematical models of ligand distribution in tissue outlined in (28, 29), simulating a tissue environment using a PDE model that incorporates four transport mechanisms: (1) free diffusion, (2) ECM binding, (3) fluid advection, (4) degradation. The spatial domain is a rectangle of size $300 \mu\text{m} \times 900 \mu\text{m}$. We model ligands being supplied through fluid flows from the left boundary of the domain, and penetrate the interstitial space between immobilized cells. Soluble ligands are then transported by diffusion and fluid flow, and become immobilized upon binding to an extracellular matrix (ECM) made up of networks of interconnected fibers containing ligand

binding sites. We explicitly represent both ECM-bound (c_b) and soluble forms of the ligand (c_s), so that the total ligand concentration $c(x, t)$ at position x and time t is equal to,

$$c(x, t) = c_s(x, t) + c_b(x, t). \quad (\text{S1})$$

Mathematically, we can describe the dynamics of the soluble fraction $c_s(x, t)$ as follows,

$$\frac{\partial c_s}{\partial t} = \kappa|_{\text{boundary}} - u(x, t) \cdot \nabla c_s + D \Delta c_s - k_{\text{ECM}}(e(x) - c_b)c_s - \gamma_s c_s. \quad (\text{S2})$$

1. The first term, κ , represents production/release of molecule at the left boundary.
2. The second term represents fluid transport, where $u(x, t)$ is the velocity field of the interstitial fluid with input flow speed u^{in} at the left boundary. We impose zero-velocity condition on the top and bottom boundary.
3. The third term represents diffusion with D as the ligand diffusion coefficient.
4. The fourth term represents ECM binding. The concentration of ECM binding site $e(x)$ at position x is generated using a minimal model of ECM protein distribution (see paragraph on "Generating ECM fiber network"). Binding occurs with rate proportional to $e(x) - c_b(x, t)$, the level of available ECM binding site. Since the on-rate of ECM binding is much larger than the off-rate, we assume the off-rate to be zero.
5. The last term represents enzymatic degradation of ligand.

The dynamics of ECM-bound fraction $c_b(x, t)$ is much simpler, involving a term corresponding to ECM binding, a degradation term due to enzymatic decay.

$$\frac{\partial c_b}{\partial t} = k_{\text{ECM}}(e(x) - c_b)c_s - \gamma_b c_b. \quad (\text{S3})$$

To generate a ligand concentration field c , we take κ to be non-zero for a brief period of time, representing a bolus of ligand released. Then, we simulate the combined dynamics of bound and soluble fractions for sufficiently long until the ligand distribution $c(x, t)$ is relatively stable. In practice, we observe that $c \approx c_b$ after a sufficiently long period of time, since the soluble fraction quickly become insignificant due to fluid flow. The resulting concentration field represents an interstitial gradient. The average concentration is set by setting the release rate κ such that the concentration of the soluble fraction c_s matches measured chemokine concentration found in interstitial fluids (1-10 pM) (30, 31).

Generating ECM fiber network To generate a distribution of ECM binding sites $e(x)$ Equation S3, we use a minimal computation model of fiber network (32–34). The model generates ECM fibers represented by line segments, which could represent fibronectin, collagen, laminin, or other fibrous matrix components. To position each fiber, one end of each segment is randomly positioned following a uniform distribution within the domain. The other end's position is determined by picking an angle, uniformly from $[0, 2\pi]$, and length sampled from a normal distribution with mean $75\mu m$ and standard deviation of $5\mu m$ (as measured for collagen by Friedl et al (35)). In total, 4050 fibers were placed in the domain. For the PDE simulation, the generated network is discretized by counting the number of fibrous proteins around each node in the simulation lattice. The density of fiber within each node is then converted to a concentration value representing the level of ECM binding sites, resulting in an average concentration of ECM binding site of 520 nM.

Numerical simulation of receptor feedback scheme

In our feedback scheme, receptor $r(x, t)$ is modeled by considering three redistribution mechanisms: (1) lateral diffusion of r along the plasma membrane ($D\nabla_{\text{memb}}^2 r$), (2) endocytosis of r along the plasma membrane ($k_{\text{off}} r$), (3) incorporation of cytoplasmic pool of receptors, R_{cyto} , to the membrane at rate proportional to local receptor activity (hAR_{cyto}). $A(x, t)$ is a random variable that denotes receptor activity along the cell membrane, and is a function of local receptor number. Then, the equation describing the distribution of r across the cell membrane can be expressed mathematically as,

$$\frac{\partial r(x, t)}{\partial t} = D\nabla_{\text{memb}}^2 r - k_{\text{off}} r + hAR_{\text{cyto}}, \quad (\text{S4})$$

where the total number of receptors $r_{\text{tot}} = \int_{\text{memb}} r + R_{\text{cyto}}$ is fixed.

We simulate receptor distribution by treating the cell membrane as a 1D space and the cytosol as a single, homogeneous compartment. This simplification allows us to simulate our PDE using the Crank-Nicolson method in one spatial dimension. Given space and time units Δx and Δt , respectively, the Crank-Nicolson method with $R_i^j := r(i\Delta x, j\Delta t)$ and $A_i^j := A(i\Delta x, j\Delta t)$ is given by the difference scheme

$$\frac{R_i^{j+1} - R_i^j}{\Delta t} = \frac{D}{2\Delta x^2} \left(R_{i+1}^j - 2R_i^j + R_{i-1}^j + R_{i+1}^{j+1} - 2R_i^{j+1} + R_{i-1}^{j+1} \right) - \frac{k_{\text{off}}}{2} \left(R_i^j + R_i^{j+1} \right) + \frac{hA_i^j}{2} \left(R_{\text{cyto}}^j + R_{\text{cyto}}^{j+1} \right) \quad (\text{S5})$$

where, $i = 1, 2, 3, \dots, m$, representing m discrete membrane compartments and R_{cyto}^j represents the additional cytosol compartment. Since the membrane is represented by a circle, we have the following pair of conditions,

$$R_0^j = R_m^j, \quad R_{m+1}^j = R_1^j. \quad (\text{S6})$$

Lastly, total receptor number across all compartments is conserved,

$$\sum_{i=1}^m R_i^j + R_{\text{cyto}}^j = \sum_{i=1}^m R_i^{j+1} + R_{\text{cyto}}^{j+1}. \quad (\text{S7})$$

Now, we can combined Equation S5-S7 and rewrite everything in vector form. First, let

$$\alpha := \frac{D}{2\Delta x^2}, \quad \beta := \frac{k_{\text{off}}}{2}, \quad \kappa_i^j := \frac{hA_i^j}{2},$$

and rewrite Equation S5 as,

$$\frac{R_i^{j+1}}{\Delta t} - \alpha \left(R_{i+1}^{j+1} - 2R_i^{j+1} + R_{i-1}^{j+1} \right) + \beta R_i^{j+1} - \kappa_i^{j+1} R_{\text{cyto}}^{j+1} = \frac{R_i^j}{\Delta t} + \alpha \left(R_{i+1}^j - 2R_i^j + R_{i-1}^j \right) - \beta R_i^j + \kappa_i^j R_{\text{cyto}}^j \quad (\text{S8})$$

and define U^j to be the $(m + 1)$ -dimensional vector with components R_i^j for $i = 1, 2, 3, \dots, m$ and $U_{m+1}^j = R_{\text{cyto}}^j$. The difference scheme is given in the vector form

$$PU^{j+1} = QU^j. \quad (\text{S9})$$

where,

$$P = \begin{bmatrix} \frac{1}{\Delta t} + 2\alpha + \beta & -\alpha & 0 & \cdots & 0 & -\alpha & -\kappa_1^{j+1} \\ -\alpha & \frac{1}{\Delta t} + 2\alpha + \beta & -\alpha & 0 & \cdots & 0 & -\kappa_2^{j+1} \\ 0 & \ddots & \ddots & \ddots & & & \vdots \\ \vdots & & \ddots & \ddots & \ddots & & \\ 0 & \cdots & 0 & -\alpha & \frac{1}{\Delta t} + 2\alpha + \beta & -\alpha & -\kappa_{m-1}^{j+1} \\ -\alpha & 0 & \cdots & 0 & -\alpha & \frac{1}{\Delta t} + 2\alpha + \beta & -\kappa_m^{j+1} \\ 1 & 1 & \cdots & & & 1 & 1 \end{bmatrix} \quad (\text{S10})$$

$$Q = \begin{bmatrix} \frac{1}{\Delta t} - 2\alpha - \beta & \alpha & 0 & \cdots & 0 & \alpha & \kappa_1^j \\ -\alpha & \frac{1}{\Delta t} - 2\alpha - \beta & \alpha & 0 & \cdots & 0 & \kappa_2^j \\ 0 & \ddots & \ddots & \ddots & & & \vdots \\ \vdots & & \ddots & \ddots & \ddots & & \\ 0 & \cdots & 0 & \alpha & \frac{1}{\Delta t} - 2\alpha - \beta & \alpha & \kappa_{m-1}^j \\ \alpha & 0 & \cdots & 0 & \alpha & \frac{1}{\Delta t} - 2\alpha - \beta & \kappa_m^j \\ 1 & 1 & \cdots & & & 1 & 1 \end{bmatrix} \quad (\text{S11})$$

Because A is invertible, the Crank-Nicolson scheme reduces to the iterative process

$$U^{j+1} = P^{-1} Q U^j. \quad (\text{S12})$$

Furthermore, we model receptor activation A_i as follows (36),

$$P(A_i | C_i, R_i) = \frac{\mu_i^{A_i}}{A_i!} e^{-\mu_i}, \quad (\text{S13})$$

where $\mu_i = R_i \frac{C_i}{K_d}$. The bracket term represents the probability of activation for a receptor experiencing C_i ligands. K_d is the equilibrium dissociation constant and α represents constitutive receptor activity, which we take to be small ($\alpha \ll 1$). In other words, the number of active receptors A_i given ligand count C_i is a Poisson random variable with mean μ_i . The entire evolution of r can be solved where at each time step, we update receptor activity A_i^j across all membrane position i according to the random process described by Equation S13, followed by solving Equation S12 for U^{j+1} .

We set the value of the feedback constant h using empirical measurements from (37). In Figure 3M of Marco et al., the authors report a quartile box plot showing estimated values for a parameter they call h (which we will refer to as \bar{h}), with a mean estimate of around 1.6e-3/s. Note \bar{h} is equivalent in meaning as our hA_i . However, since hA_i will be different across different membrane bins and across time, we simulate the feedback scheme for a cell in a given environment and set the value of h such that the mean rate $\langle hA_i \rangle$ (averaged across membrane and time) is approximately equal to the mean estimate of 1.6e-3/s reported by Marco et al.. The value \bar{h} reported by Marco et al. corresponds specifically to the transport rate of the Cdc42 to the membrane. The parameter value

was obtained by analyzing fluorescence recovery of GFP-Cdc42 in membrane regions bleached with a laser pulse. Although the measured value corresponds to Cdc42, it has been used to model the effective exocytosis rate for receptors shown to undergo activity-dependent localization, showing good agreement with empirical data (38). Similar values around 1-2e-3/s have been measured for the recycling rate of a wide range of GPCRs (39–42).

Numerical simulation of Local Excitation and Global inhibition

We simulate a Local Excitation, Global Inhibition Biased Excitable Network (LEGI-BEN) as described by Shi et al. (43). This model implements an excitable network module based on an activator-inhibitor system, where stochastic fluctuations initiate activity. The dynamics are governed by the following equations:

$$\begin{aligned}\frac{\partial X}{\partial t} &= D_X \nabla^2 X + k_{XX} \frac{X^2}{k_M^2 + X^2} - k_{-X} X - k_{YX} Y + k_{UX} U \\ \frac{\partial Y}{\partial t} &= D_Y \nabla^2 Y + k_{XY} X - k_{-Y} Y\end{aligned}\quad (\text{S14})$$

Here, U serves as the input to the excitable system and includes contributions from three components: basal activation (B), stochastic fluctuations (N), and the response regulator (R) from the LEGI module, as shown below:

$$U = B + N + \lambda (R - R_{\text{init}}). \quad (\text{S15})$$

The LEGI module processes the stimulus (S) to drive the response regulator (R), which biases the activity of the excitable network. Its dynamics are described by the following system:

$$\begin{aligned}\frac{\partial E}{\partial t} &= -k_{-E} E + k_E S \\ \frac{\partial I}{\partial t} &= -k_{-I} I + k_I S + D_I \nabla^2 I \\ \frac{\partial R}{\partial t} &= -k_{-R} I R + k_R (R_T - R) E\end{aligned}\quad (\text{S16})$$

In this framework, the activity of Y determines the direction of cell migration, with cells moving toward the region of maximal Y activity on their surface.

All simulations and the model implementation were carried out in MATLAB (44), closely following the protocol in (43). The signaling partial differential equations (PDEs) were solved on

a one-dimensional representation of the cell boundary, using periodic boundary conditions. The spatial domain was discretized into 360 points, and spatial diffusion terms were approximated with central finite differences. This discretization transforms the PDEs into ordinary differential equations (ODEs), which were solved using the SDE toolbox in MATLAB. Simulations were run with a time step of 0.025 seconds.

Simulation of cell navigation

Haptotaxis algorithm At $t = 0$, initialize a cell at position $p_0 \in \Omega \subset \mathbb{R}^2$.

At each subsequent time step $t = t + \Delta t$ with the cell at position $p_t \in \Omega$:

1. Compute mean ligand profile $\mathbf{c} \in \mathbb{R}^m$ at the cell's current position.
2. Independently sample n ligand profiles $\{\mathbf{C}^{(i)}\}_{i=1}^n$ where each element C_j is distributed as a Poisson random variable with mean equal to c_j .
3. For each ligand profile $\mathbf{C}^{(i)}$ sampled, sample a corresponding receptor activity profiles $\mathbf{A}^{(i)}$,

$$\mathbf{A}^{(i)} | \mathbf{C}^{(i)} \sim \prod_{j=1}^m \text{Pois}(\lambda_j), \text{ where } \lambda_j = r_j \left(\frac{C_j^{(i)}}{C_j^{(i)} + K_d} + \alpha \frac{K_d}{C_j^{(i)} + K_d} \right). \quad (\text{S17})$$

4. Select the next direction $\hat{\theta}$ as the direction of maximal receptor activity or belief probability in the case of Bayes filtering.
5. Set new cell position $p_{t+\Delta t} = p_t + s\Delta t [\cos(\hat{\theta}), \sin(\hat{\theta})]$, with speed $s = 1\mu\text{m}/\text{min}$, $\Delta t = 1\text{s}$.
6. Repeat from step 1.

Robot navigation simulation

Environment setup We implemented an (Extended) Kalman filtering approach for target navigation where a robot localizes and moves toward a target using noisy signal measurements. A Kalman filter is a special type of Bayes filter where both the motion and measurement noise are Gaussian and are more amenable to analytical treatments. The environment is discretized into a 100×100 grid, with the robot starting at (25, 25) and the target positioned at coordinates (75, 75). The target emits a signal that decays with distance according to an inverse power law:

$$h(x) = \frac{s_{\max}}{\|x - x_{\text{target}}\|^{\gamma}} \quad (\text{S18})$$

where $s_{\max} = 0.2$ is the maximum signal strength and $\gamma = 0.3$ is the decay exponent. The actual measured signal z_t is a noisy version of $h(x)$,

$$z_t = h(x) + \epsilon_t, \quad \epsilon_t \sim \mathcal{N}(0, \alpha^2). \quad (\text{S19})$$

Robot action The robot maintains a belief state $b_t(x)$ representing a probability distribution over possible target locations which gets updated per unit time. At each iteration, the robot updates its belief by observing a signal at its own grid position $r(t)$ in the arena, and moves in the direction of the maximum likelihood target location:

$$u_t = \lambda \frac{r(t) - \arg \max_x b_t(x)}{\|r(t) - \arg \max_x b_t(x)\|} \quad (\text{S20})$$

where λ is the movement step size. The robot's actual motion includes Gaussian noise with standard deviation 0.5.

Belief update The robots' belief $b_t(x)$ is updated in two stages: motion update and measurement update. The motion update incorporates robot movement uncertainty through a 2D convolution operation:

$$b_{t+1}(x) = b_t(x) * K_{\sigma(s)} \quad (\text{S21})$$

where $*$ denotes 2D convolution and $K_{\sigma(s)}$ is a 5×5 Gaussian kernel with scalar standard deviation $\sigma(s)$. Each kernel element (i, j) is computed as:

$$K_{\sigma(s)}(i, j) = \exp\left(-\frac{d_{ij}^2}{2\sigma(s)^2}\right) \quad (\text{S22})$$

where d_{ij} is the Euclidean distance from position (i, j) to the kernel center, and the kernel is normalized to sum to 1.

For the adaptive strategy, the motion uncertainty $\sigma(s)$ varies with signal strength:

$$\sigma(s) = D_{\text{base}} + (D_{\text{true}} - D_{\text{base}})e^{-ks} \quad (\text{S23})$$

where $D_{\text{base}} = 0.1$ is the minimum uncertainty, $D_{\text{true}} = 0.5$ matches the true motion variability of the robot, and $k = 2.0$ is the decay rate. In the non-adaptive strategy, uncertainty remains fixed at the true motion variability of 0.5.

The measurement update applies Bayes' rule using a Gaussian likelihood model:

$$b_{t+1}(x) = \eta \cdot b_t(x) \cdot \exp\left(-\frac{(z_t - h(x))^2}{2\alpha^2}\right) \quad (\text{S24})$$

where z_t is the signal strength measured by the robot at its position $r(t)$, $h(x)$ is the expected signal strength at $r(t)$ if the target is located at x , and η is a normalization factor ensuring the belief sums to 1.

Performance Evaluation We compared adaptive and non-adaptive strategies through multiple simulation runs across environments with different signal-to-noise ratio (SNR). A run was considered successful if the robot reached within 5.0 grid units of the target. Both strategies were evaluated using identical random seeds for paired comparison. Paired t-tests used to assess statistical significance of the observed differences in steps to target.

Understanding adaptive strategy based on Kalman gain We can understand the effectiveness of the adaptive strategy by studying the gain of a 1-D Kalman filter. The Kalman gain (K_t) controls how much weight is given to a new measurement relative to the current belief, defined as:

$$K_t = \frac{\sigma_{t|t-1}^2}{\sigma_{t|t-1}^2 + \sigma_x^2}, \quad (\text{S25})$$

where σ_x^2 is the uncertainty in the estimated target position x and $\sigma_{t|t-1}^2$ is the predicted belief variance after the motion step.

To relate uncertainty in the signal $h(x)$ to σ_x^2 , we use the error propagation formula,

$$\begin{aligned} \sigma_x^2 &= \left(\frac{dx}{dh}\right)^2 \sigma_h^2 \\ &= \left(\frac{dx}{dh}\right)^2 \alpha^2 \\ &= \frac{\alpha^2}{\gamma^2 s_{\max}^2} \cdot \|x - x_{\text{target}}\|^{2(\gamma+1)}. \end{aligned}$$

Furthermore, the variance term after motion update $\sigma_{t|t-1}^2$ is the sum of the posterior variance from the previous step and the variance of the motion model:

$$\sigma_{t|t-1}^2 = \sigma_t^2 + \sigma_p^2. \quad (\text{S26})$$

Recall $\sigma_p^2 = \sigma(s)^2$ decreases as the signal s becomes stronger according to Equation S23.

Combining Equation S25 and Equation S26, we rewrite the Kalman gain:

$$K_t = \frac{\sigma_t^2 + \sigma_p^2}{\sigma_t^2 + \sigma_p^2 + \sigma_x^2}. \quad (\text{S27})$$

The Kalman gain takes a value between 0 and 1, where a larger gain means that new measurements are weighted more heavily relative to the prior belief.

When the robot is initially far from the target, the SNR is low, making the prior unreliable. However, because the target is distant, the position uncertainty σ_x^2 is also large, which naturally leads to a small Kalman gain K_t . By increasing the motion model variance σ_p^2 , we increase K_t , making the filter more responsive to new measurements and preventing it from getting stuck relying too heavily on an uncertain prior.

As the robot moves closer to the target, the SNR improves, and the Kalman gain naturally increases as σ_x^2 decreases. If K_t remains too large, the filter may overreact to measurement noise, leading to unstable belief updates. By reducing σ_p^2 , the Kalman gain decreases, allowing the filter to trust past observations more, which stabilizes convergence.

Finally, the dependence of K_t on the motion model variance σ_p^2 is mediated by σ_x^2 . When σ_x^2 is small, Equation S27 shows that the Kalman gain approaches 1, making it independent of σ_p^2 . This explains why the adaptive strategy provides the greatest advantage in noisy environments, where large σ_x^2 causes inefficient belief updates if σ_p^2 is not properly adjusted.